Kinematics Modeling of a Wheel-Based Pole Climbing Robot (UT-PCR)

Ali Baghani Majid Nili Ahmadabadi Ahad Harati
Robotics and AI Lab, Control and Intelligent Processing Center of Excellence, Department of Electrical and Computer Engineering, University of Tehran
a.baghani@ece.ut.ac.ir *mnili@ut.ac.ir*

***Abstract* - This paper is concerned with the derivation of the kinematics model of the University of Tehran-Pole Climbing Robot (UT-PCR). As the first step, an appropriate set of coordinates is selected and used to describe the state of the robot. Nonholonomic constraints imposed by the wheels are then expressed as a set of differential equations. By describing these equations in terms of the state of the robot an underactuated driftless nonlinear control system with affine inputs that governs the motion of the robot is derived. A set of experimental results are also given to show the capability of the UT-PCR in climbing a stepped pole.**

***Index Terms* – Climbing robot, wheel-based, kinematics modeling, nonholonomic constraints, singularity.**

I. Introduction

Climbing robots have various applications in industrial and hazardous environments. Inspection of vertical and inclined pipes in nuclear power plants, wiring on high voltage power transmission towers, and inspection of high chimneys are some well known examples of such applications [1, 2]. Moreover, some new and important tasks for climbing robots can be introduced. Cleaning electric lights on lampposts in highways is one of these new tasks.

Air pollution in metropolitan areas is the main cause of dirt on highway light bulbs. Therefore, the highway lighting systems should be cleaned on regular bases in order to have the required light in the highways without resorting to more powerful and energy consuming lighting systems.

Manual cleaning of highway lighting systems is a very dangerous and traffic disturbing task. Therefore, Robotics and Artificial Intelligence Laboratory of the University of Tehran is currently engaged in the development of a wheel-based pole climbing robot named University of Tehran-Pole Climbing Robot (UT-PCR), see Fig. 1. The UT-PCR is light weight, fail-safe, relatively fast, nonholonomic and therefore underactuated, and is designed for climbing stepped poles with circular or near circular cross sections [3]. The climbing part of the UT-PCR consists of a triangular body and six limbs with ordinary wheels at their tips. Three lower wheels are actuated with DC motors. The upper limbs have passive wheels and act just to increase the system stability.

In [3] related robots and the natural and artificial climbing mechanisms are reviewed and the design of the UT-PCR is described. As the first step towards nonholonomic path planning and control of the UT-PCR, in this paper, a set of suitable generalized coordinates for the climbing mechanism is identified. Then by considering the nonholonomic constraints on the wheels, the inverse kinematics model of the climbing part is developed and the robot's singular configurations are found numerically. Some experimental results are also given to show the climbing capability of UT-PCR using a simple control system.

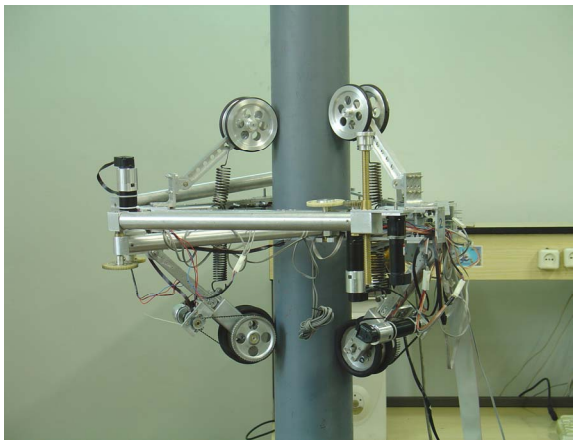

Fig. 1 The University of Tehran Pole Climbing Robot

II. Assumptions and Notation

To derive a set of differential equations describing the motion of the robot with the wheel velocities as the affine inputs, a number of assumptions have been made in the modeling. The UT-PCR as shown in Fig. 1 is over-constrained, as will become apparent in the following sections. The three upper limbs only serve to increase the stability of the robot against tip-over and improve the grasp of the robot on the pole. Hence the wheels on these limbs should not add any constraints to the motion of the robot. Using holonomic passive wheels on these limbs will serve this goal. Although at this stage of development we have used ordinary passive wheels, we will assume that these wheels are holonomic and therefore the upper limbs can be neglected in the kinematics modeling.

Moreover we have assumed that the forces exerted by the springs produce large enough normal components to bring the lower wheels in good contact with the surface of the pole so that the wheels do not slip. This enables us to

use the classical model for the wheel constraints [4].

Finally we have assumed that the distance from each corner of the body to the contact point of its wheel with the pole is constant, no matter what the configuration of the robot is. This is a valid approximation when the radius of the wheel is much smaller than the length of the limb.

Based on these assumptions the UT-PCR can simply be represented as shown in Fig. 2. The *corner points* of the body are denoted by C_1, C_2 and C_3 while the corresponding *contact points* of the wheels with the cylindrical pole by W_1, W_2 and W_3. By the word *body* we are referring to the triangle $C_1C_2C_3$, whose *sides* are C_1C_2, C_1C_3 and C_2C_3. The *limbs* are the segments C_1W_1, C_2W_2 and C_3W_3.

In the following sections we use different sets of coordinates to describe the position of points of interest. The z-axis of the Cartesian coordinate system is assumed to be aligned with the axis of the cylinder. We use the notation $\vec{A}$ to indicate the vector from the origin to point A. If the Cartesian coordinates of A is denoted by $(x_A \quad y_A \quad z_A)$, $\vec{A}$ can be written as

$$\vec{A} = [x_A \quad y_A \quad z_A]^T . \tag{1}$$

The cylindrical and spherical coordinates of A are respectively denoted by $(r_A \quad \phi_A \quad z_A)$ and $(R_A \quad \theta_A \quad \phi_A)$.

We use the notation $\overrightarrow{AB}$ to indicate the vector from point A to point B hence

$$\overrightarrow{AB} = \vec{B} - \vec{A} . \tag{2}$$

The length of the body sides, the limbs and the radius of the cylinder are respectively denoted by b, l and r, as shown in Fig. 3.

III. Dimension of the State Manifold

We claim that the state space of the UT-PCR has a dimension of six. As the first step in the proof, the behavior of the joints is scrutinized. The joints connecting the limbs to the body at the corner points are 1 DOF revolute joints (hinges). Depicted in Fig. 4 is the locus of W_1 as the angle of the joint at C_1 varies, which is a circle of radius l centered at C_1. By the symmetrical design of the UT-PCR, the plane in which this circle lies is the perpendicular bisector plane of the body side $\overline{C_2C_3}$. As a result in addition to C_1, this plane passes through the midpoint of $\overline{C_2C_3}$, denoted by M_{23}. The loci of W_2 and W_3 are similarly found. In general words, W_i moves in the perpendicular bisector plane of $\overline{C_jC_k}$,

$$\overrightarrow{C_jC_k} \cdot \overrightarrow{C_iW_i} = 0 , \tag{3}$$

and its distance from C_i is equal to l,

$$\left\| \overrightarrow{C_iW_i} \right\| = l . \tag{4}$$

Moreover we have:

$$\overrightarrow{C_jC_k} \cdot \overrightarrow{C_iM_{jk}} = 0 . \tag{5}$$

Now we consider the body triangle with the limbs stretched apart from the pole. As a solid object in the 3D space the body has six degrees of freedom [5]. Therefore one parameterization to describe the configuration of the body consists of the Cartesian coordinates of the center of the body triangle together with its Euler angles:

$$\underline{X}_b = [x_{CM} \quad y_{CM} \quad z_{CM} \quad \phi \quad \theta \quad \psi]^T . \tag{6}$$

If we release the stretched limbs, their springs pull them back towards the pole and they touch the surface of the pole. This is a deterministic process. Therefore the aforementioned parameterization can well be chosen as the state of the robot.

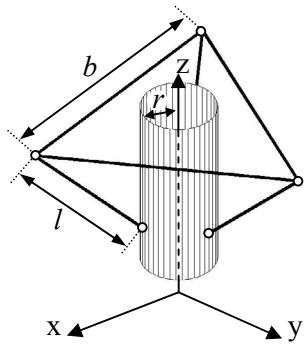

Fig. 3 The coordinate system and mechanical dimensions

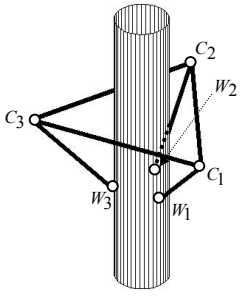

Fig. 2 The simplified model of the UTPCR

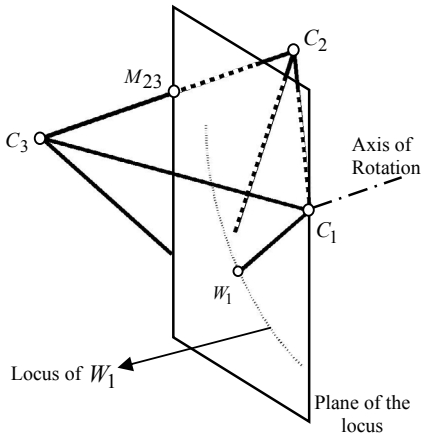

Fig. 4 The locus of W_1 as the angle of the joint of limb C_1W_1 varies

Mathematically the contact point W_i is the intersection of the circle defined by (3) and (4) , with the cylindrical section which is obtained by cutting the pole with the plane of the locus, as defined by (3). This section is an ellipse in general, hence we have the intersection of a circle with an ellipse, which can be expressed as a fourth order equation in one variable (Fig. 5). This equation has at most four solutions for a given $\underline{X}_b$, two of which correspond to points on the opposite side of the cylinder (points No.1 and 2 in Fig. 5), which are not physically feasible, because the limbs cannot pass through the cylinder. Of the remaining two solutions, one corresponds to a point whose z coordinate is greater than the corresponding corner of the body (point No.3 in Fig. 5). Because the limbs cannot move above the body, this solution is also rejected. Hence only one of these solutions is the point we are interested in, i.e. the position of W_i (point No.4 in Fig. 5). Since the contact points W_i are located on the surface of the cylinder, the z and ϕ components of the cylindrical coordinates of these points, give a complete description of their configuration:

$$\underline{X}_w = \begin{bmatrix} z_{W_1} & \phi_{W_1} & z_{W_2} & \phi_{W_2} & z_{W_3} & \phi_{W_3} \end{bmatrix}^T . \quad (7)$$

Thus we have shown that the positions of the contact points $\underline{X}_w$ as described by (7) can uniquely be obtained from the state of the body $\underline{X}_b$ as described by (6), i.e.

$$\underline{X}_w = \underline{f}_{IK}(\underline{X}_b) . \quad (8)$$

This proves that the UTPCR has a six dimensional state manifold and as noted earlier (6) can be chosen as the state of the robot.

$\underline{X}_b$ contains the parameters to be controlled while $\underline{X}_w$ contains the parameters to be actuated, hence we may call the function $\underline{f}_{IK}$ the inverse kinematics of the UT-PCR [6]. In the next section we shall choose another set of parameters as the state to facilitate numerical calculations.

IV. State selection

In this section our aim is to select an appropriate set of parameters as the state which exploits the symmetries present in the system to simplify numerical calculations. We are particularly interested in the relative configuration of the robot with respect to the pole. It is easy to see that a translation in the z coordinates of all the wheels does not change this configuration as is the case with a rotation in their ϕ coordinates. To benefit from these symmetries we will choose the coordinates of one of the wheels as the base on which we shall construct the robot. In this way the relative configuration of the robot with respect to the pole is preserved under a translation or rotation in its base.

In Fig. 6 a simplified representation of the robot is shown. We claim that as long as the points W_1 , C_1 and M_{23} form a plane, $\underline{X}_b$ is uniquely determined by, and uniquely determines the positions of these points. If $\underline{X}_b$ is known, $\overrightarrow{C_1}$, $\overrightarrow{C_2}$ and $\overrightarrow{C_3}$ are known, so is $\overrightarrow{M_{23}}$. By the process explained in section 3 $\overrightarrow{W_1}$ can also be found. This proves the second part of the claim. To prove the first part it suffices to show that $\overrightarrow{C_2}$ and $\overrightarrow{C_3}$ can be expressed in terms of the coordinates of these points. From (3) and (5):

$$\overrightarrow{C_2C_3} \cdot \overrightarrow{C_1M_{23}} = 0 \quad (9)$$

$$\overrightarrow{C_2C_3} \cdot \overrightarrow{C_1W_1} = 0 . \quad (10)$$

While the lengths of $\overline{C_2M_{23}}$ and $\overline{C_3M_{23}}$ are equal to $\frac{b}{2}$,

$$\overrightarrow{C_2M_{23}} \cdot \overrightarrow{C_2M_{23}} = \frac{b^2}{4} \quad (11)$$

$$\overrightarrow{C_3M_{23}} \cdot \overrightarrow{C_3M_{23}} = \frac{b^2}{4} . \quad (12)$$

By solving these equations the coordinates of C_2 and C_3 are found as

$$\overrightarrow{C_2} = \overrightarrow{M_{23}} + \frac{b}{2} \cdot \frac{\overrightarrow{C_1W_1} \times \overrightarrow{C_1M_{23}}}{\left\| \overrightarrow{C_1W_1} \times \overrightarrow{C_1M_{23}} \right\|} \quad (13)$$

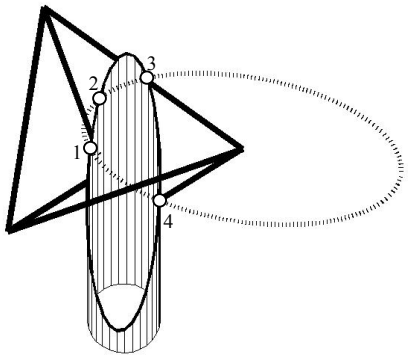

Fig. 5 The solutions of the inverse kinematics for W_i

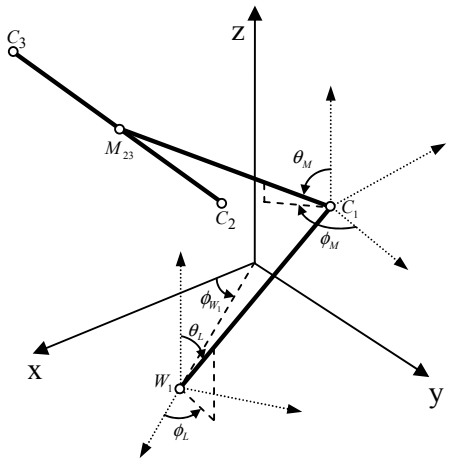

Fig. 6 The selected parameters

$$\overrightarrow{C_3} = \overrightarrow{M_{23}} - \frac{b}{2} \cdot \frac{\overrightarrow{C_1W_1} \times \overrightarrow{C_1M_{23}}}{\left\| \overrightarrow{C_1W_1} \times \overrightarrow{C_1M_{23}} \right\|}. \quad (14)$$

This completes the proof. Based on this, if we choose a set of parameters which determines $\overrightarrow{W_1}$, $\overrightarrow{C_1}$ and $\overrightarrow{M_{23}}$ with a one to one correspondence, we can well use it as the state of the robot instead of $\underline{X}_b$.

Referring to Fig. 6, we have chosen z_{W_1} and ϕ_{W_1} as the first two components of this set. The spherical angles of C_1 relative to a basis whose origin is at W_1 and whose x and y axes have been rotated by an angle of ϕ_{W_1} are chosen as the next two components. These coordinates are denoted by θ_L and ϕ_L. The last two components are the spherical angles of M_{23} relative to a basis whose origin is at C_1 and whose x and y axes have been rotated by an extra angle of ϕ_L. These coordinates will be denoted by θ_M and ϕ_M. The Cartesian coordinates of W_1, C_1 and M_{23} can be written as

$$\overrightarrow{W_1} = \begin{bmatrix} r \cdot \cos(\phi_{W_1}) \\ r \cdot \sin(\phi_{W_1}) \\ Z_{W_1} \end{bmatrix} \quad (15)$$

$$\overrightarrow{C_1} = \overrightarrow{W_1} + \begin{bmatrix} l \cdot \sin(\theta_L) \cdot \cos(\phi_L + \phi_{W_1}) \\ l \cdot \sin(\theta_L) \cdot \sin(\phi_L + \phi_{W_1}) \\ l \cdot \cos(\theta_L) \end{bmatrix} \quad (16)$$

$$\overrightarrow{M_{23}} = \overrightarrow{C_1} + \frac{\sqrt{3}}{2} \begin{bmatrix} b \cdot \sin(\theta_M) \cdot \cos(\phi_M + \phi_L + \phi_{W_1}) \\ b \cdot \sin(\theta_M) \cdot \sin(\phi_M + \phi_L + \phi_{W_1}) \\ b \cdot \cos(\theta_M) \end{bmatrix}. \quad (17)$$

If we collect the selected parameters in $\underline{X}_s$,

$$\underline{X}_s = \begin{bmatrix} z_{W_1} & \phi_{W_1} & \theta_L & \phi_L & \theta_M & \phi_M \end{bmatrix}^T \quad (18)$$

and we have shown that

$$\underline{X}_b = \underline{g}(\underline{X}_s) \quad (19)$$

where g is an invertible function. Hereafter by the state of the UT-PCR we are referring to $\underline{X}_s$. Using (8) we have

$$\underline{X}_w = \underline{f}_{IK}(\underline{g}(\underline{X}_s)). \quad (20)$$

V. Nonholonomic Constraints

The nonholonomic constraints arise from the fact that a wheel in contact with a surface can only move in one direction [4]. The line along which the wheel can move is the intersection of the tangent plane to the surface at the point of contact with the plane of the wheel (the wheel is modeled as a disk and the plane of the wheel is the plane of that disk). These planes are shown in Fig. 7 for a wheel of the UT-PCR (W_1). The tangent plane is a vertical plane tangent to the pole at the point of contact. The plane of the wheel is determined by the geometry of the design. For the UT-PCR this is the plane which passes through the point

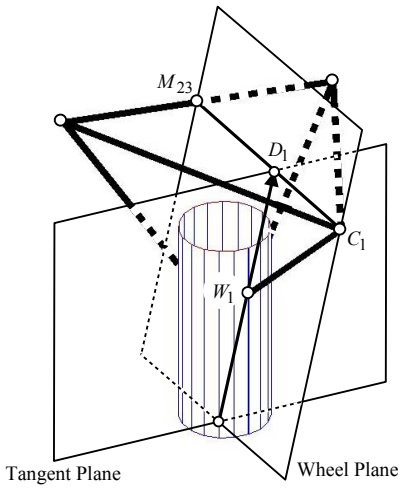

Fig. 7 The direction of motion for W_1

of contact of the wheel W_1, the corner of the body corresponding to that wheel C_1, and the midpoint of the opposite side of the body M_{23}. The line segment $\overline{C_1M_{23}}$ lies in this plane, so that its intersection with the tangent plane, as denoted by D_1, lies on both planes. Hence the line of intersection of the two planes includes $\overline{W_1D_1}$ as a segment and this line segment determines the direction of motion for W_1. The directions of motion for the other two wheels can also be determined (using a similar notation by line segments $\overline{W_2D_2}$ and $\overline{W_3D_3}$).

The position of D_1 can be expressed in terms of the state:

$$\overrightarrow{D_1} = \alpha \cdot \overrightarrow{C_1} + (1-\alpha) \cdot \overrightarrow{M_{23}}, \quad (21)$$

$$\begin{bmatrix} x_{W_1} & y_{W_1} & 0 \end{bmatrix} \cdot \overrightarrow{W_1D_1} = 0. \quad (22)$$

The former equation simply states that D_1 lies on $\overline{C_1M_{23}}$ while the latter states that it belongs to the tangent plane to the cylinder at W_1. Solving for $\overrightarrow{D_1}$ we have

$$\overrightarrow{D_1} = \begin{bmatrix} r^2(x_{M_{23}} - x_{C_1}) \\ + y_{W_1}(x_{C_1}y_{M_{23}} - y_{C_1}x_{M_{23}}) \\ \hline x_{W_1}(x_{M_{23}} - x_{C_1}) \\ + y_{W_1}(y_{M_{23}} - y_{C_1}) \\ r^2(y_{M_{23}} - y_{C_1}) \\ - x_{W_1}(x_{C_1}y_{M_{23}} - y_{C_1}x_{M_{23}}) \\ \hline x_{W_1}(x_{M_{23}} - x_{C_1}) \\ + y_{W_1}(y_{M_{23}} - y_{C_1}) \\ r^2(z_{M_{23}} - z_{C_1}) \\ - x_{W_1}(x_{C_1}z_{M_{23}} - z_{C_1}x_{M_{23}}) \\ + y_{W_1}(z_{C_1}y_{M_{23}} - y_{C_1}z_{M_{23}}) \\ \hline x_{W_1}(x_{M_{23}} - x_{C_1}) \\ + y_{W_1}(y_{M_{23}} - y_{C_1}) \end{bmatrix}. \quad (23)$$

The variables appearing on the right hand side are all functions of $\underline{X}_s$ described by (15), (16) and (17).

By choosing $\underline{X}_w$ from (7) as the coordinates describing the loci of the wheels on the cylinder, the nonholonomic constraints can be derived. Fig. 8 shows the tangent plane at W_i. The coordinate axes chosen are $\hat{z}_{W_i}$ and $\hat{\phi}_{W_i}$ where $\hat{z}_{W_i}$ is parallel to the z-axis of the Cartesian system and $\hat{\phi}_{W_i}$ is parallel to its xy-plane. Denoting the linear velocity of W_i by v_i we have:

$$\dot{z}_{W_i} = \frac{z_{D_i} - z_{W_i}}{\sqrt{(x_{D_i} - x_{W_i})^2 + (y_{D_i} - y_{W_i})^2 + (z_{D_i} - z_{W_i})^2}} \cdot v_i, \quad (24)$$

$$\dot{\phi}_{W_i} = \frac{1}{r} \cdot \sqrt{\frac{(x_{D_i} - x_{W_i})^2 + (y_{D_i} - y_{W_i})^2}{(x_{D_i} - x_{W_i})^2 + (y_{D_i} - y_{W_i})^2 + (z_{D_i} - z_{W_i})^2}} \cdot v_i \,. \quad (25)$$

Substituting for the coordinates of D_i and W_i in terms of the state using (23) and (20), we can write these equations in matrix form as

$$\begin{bmatrix} \dot{z}_{W_1} \\ \dot{\phi}_{W_1} \\ \dot{z}_{W_2} \\ \dot{\phi}_{W_2} \\ \dot{z}_{W_3} \\ \dot{\phi}_{W_3} \end{bmatrix} = \begin{bmatrix} f_{t_{11}}(\underline{X}_s) \\ f_{t_{21}}(\underline{X}_s) \\ 0 \\ 0 \\ 0 \\ 0 \end{bmatrix} \cdot v1 + \begin{bmatrix} 0 \\ 0 \\ f_{t_{23}}(\underline{X}_s) \\ f_{t_{24}}(\underline{X}_s) \\ 0 \\ 0 \end{bmatrix} \cdot v2 + \begin{bmatrix} 0 \\ 0 \\ 0 \\ 0 \\ f_{t_{35}}(\underline{X}_s) \\ f_{t_{36}}(\underline{X}_s) \end{bmatrix} \cdot v3 \cdot \quad (26)$$

In the compact form we have:

$$\dot{\underline{X}}_w = \underline{f}_{t_1}(\underline{X}_s) \cdot v1 + \underline{f}_{t_2}(\underline{X}_s) \cdot v2 + \underline{f}_{t_3}(\underline{X}_s) \cdot v3 \cdot \quad (27)$$

Under proper conditions this equation can be turned into a state space equation: $\dot{\underline{X}}_w$ can be expressed in terms of $\dot{\underline{X}}_s$ using the Jacobian of (20), so that

$$J \cdot \dot{\underline{X}}_s = \underline{f}_{t_1}(\underline{X}_s) \cdot v1 + \underline{f}_{t_2}(\underline{X}_s) \cdot v2 + \underline{f}_{t_3}(\underline{X}_s) \cdot v3 \cdot \quad (28)$$

The next step needed to be taken is to invert the Jacobian

$$\begin{aligned} \dot{\underline{X}}_s &= J^{-1} \cdot \underline{f}_{t_1}(\underline{X}_s) \cdot v1 + J^{-1} \cdot \underline{f}_{t_2}(\underline{X}_s) \cdot v2 + J^{-1} \cdot \underline{f}_{t_3}(\underline{X}_s) \cdot v3 \\ &= \underline{f}_1(\underline{X}_s) \cdot v1 + \underline{f}_2(\underline{X}_s) \cdot v2 + \underline{f}_3(\underline{X}_s) \cdot v3 \cdot \end{aligned} \quad (29)$$

The question of invertability of the Jacobian matrix is addressed in the next section. As is apparent, (29) is the desired state space description.

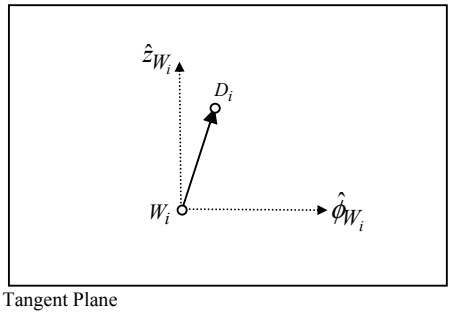

Fig. 8 The tangent plane at W_i

VI. KINEMATICS SINGULARITIES

Studies on similar platforms has established that these systems may have singularities in their forward and inverse kinematics [7]-[9]. This is also true for the UT-PCR, as our simulations show, but only occurs away from the equilibrium point. Therefore if the state of the robot is properly bounded, the robot will not enter these zones.

The dimensions used for the simulation are the true dimensions of the robot and pole, namely: b = 550mm, l = 350mm and r = 80mm. The equilibrium point, is the point where the body triangle is horizontal and its center is located on the axis of the pole, i.e.

$$\underline{X}_s(eq) = \left[0 \quad 0 \quad \sin^{-1}\left(\frac{550 \cdot \sqrt{3}/2 \cdot 2/3 - 80}{350} \right) \quad 0 \quad \frac{\pi}{2} \quad \pi \right]^T . \quad (30)$$

As a measure of singularity for the Jacobian matrix, the ratio of its largest eigenvalue to its smallest, commonly known as the condition number, was chosen. The larger the value of this function, the closer the Jacobian to a singular matrix. Fig. 9 shows the condition number as each of the coordinates are varied around the equilibrium point. We have used the gradient method to find its local maxima. The region of interest is the 4-cell (4 dimensional cube) centered at the equilibrium point with each side equal to 0.2 radians. This is equivalent to a variation of at most 5 degrees in each of the state angles. (Due to symmetry the first two coordinates of the state are of no significance and are ignored.) All corner points of a $5\times5\times5\times5$ grid in this region were used as initial points. It has been proved numerically that the maxima occur on the boundary and therefore the Jacobian is invertible in this region.

Fig. 10 depicts the condition number as θ_M varies over a wider range. As can be seen singularities are observed. It has been proved numerically that the singularities form a 5-dimensional submanifold of the 6-dimensional state space, i.e. by loosing one of its degrees of freedom, the robot can be posed in a continuous set of states, in all of which the Jacobian matrix is singular.

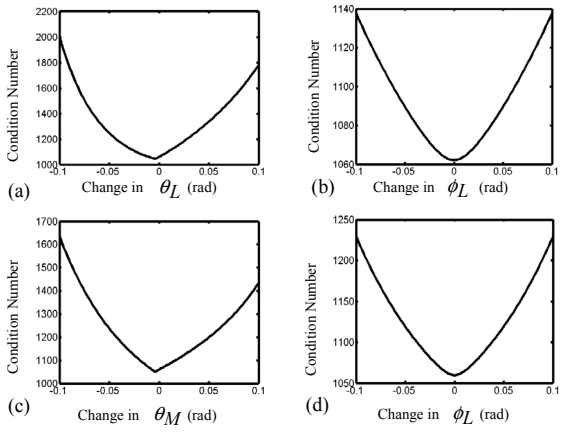

Fig. 9 The condition number as (a) θ_L (b) ϕ_L (c) θ_M (d) ϕ_M varies around the equilibrium point

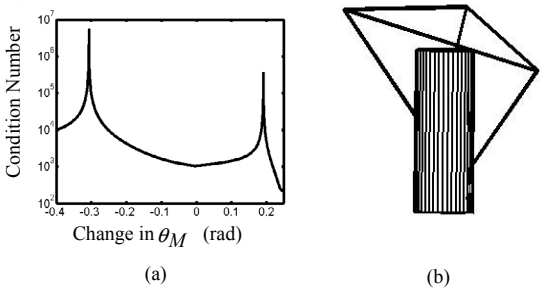

Fig. 10 (a) Singularities in the Jacobian matrix
(b) A typical singular posture

VII. Conclusions and Future Research

In this paper the kinematics model of the UT-PCR was derived. The dimension of its state space was determined and an appropriate set of coordinates were chosen to parameterize this space. By using the nonholonomic constraints imposed by the wheels, an underactuated driftless nonlinear control system (29) with the wheel velocities as the affine inputs was obtained.

The presence of singularities was also studied. In the literature classification of singularities has also been of concern (see e.g. [10]). Of particular interest are two cases; In the first case the range of the Jacobian matrix may not include the control-input vector field (the right hand side of (28)). In this case a certain combination of inputs acts contrary to the constraints and may lead to sideway slipping of the wheels. In the second case, there may exist a singular path in the state space on which the robot has free uncontrolled motion. Special measures should be taken to avoid these cases in controlling the UT-PCR if they exist. These issues are to be studied in more depth in future research.

In the experimentation, we have used PID controllers for the DC motors, and the capability of the robot to climb a stepped pole has been tested. A filmstrip of the operation is shown in Fig. 11. Performing complex motions using nonholonomic path planning is our goal in future research.

Acknowledgment

This research is financially supported by Iranian Electrical Power Generation, Distribution, and Transmission Company (TAVANIR Co.). The authors wish to thank Mr. Gh. Rajabi of TAVANIR Co. for the fruitful discussions. The authors are also thankful to Dr. Soltani, Mr. B. Yazdani, Mr. B. Moaveni and Mr. P. Sharif Kashani for their assistance in developing the robot.

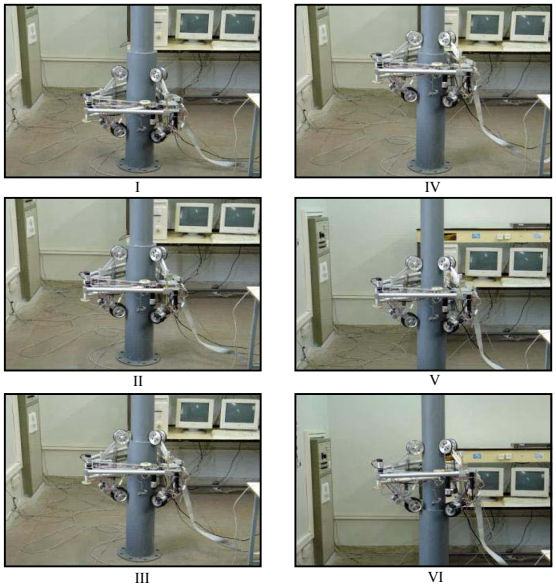

Fig. 11 Operation of the UT-PCR

References

[1] D. Bevly, Steven D. and C. Mavroidis, "A Simplified Cartesian-Computed Torque Controller for Highly Geared Systems and Its Application to an Experimental Climbing Robot," *Journal of Dynamic Systems, Measurement and Control, Trans. ASME*, Vol. 122, No. 1, pp. 27-32, 2000.

[2] R. D. Schraft, J. G. Neugebauer and Gernot Schmierer, "A modular construction system for lightweight multipurpose climbing robots," *Pro. Int. Conf. Field and Service Robotics, Pittsburgh, PA*, pp. 353-358, 1999.

[3] B. Yazdani, M. Nili Ahmadabadi, A. Harati, H. Moaveni and N. Soltani, "Design and development of a pole climbing robot mechanism," in *the proceedings of Mechatronics and Robotics, Germany,* Sep. 2004.

[4] H. Goldstein, *Classical Mechanics,* 2nd ed., Addison-Wesley, 1980, p. 14-15.

[5] H. Goldstein, *Classical Mechanics,* 2nd ed., Addison-Wesley, 1980, pp. 128-129.

[6] Y. Nakamura, *Advanced Robotics, Redundancy and Optimization*, Addison-Wesley, 1990.

[7] J. Angeles, G. Yang and I-Ming Chen, "Singularity analysis of three-legged, six-DOF platform manipulators with URS legs," *IEEE/ASME Trans. on Mechatronics,* vol. 8, no. 4, pp. 469-475, December 2003.

[8] N. Simaan and M. Shoham, "Singularity analysis of a class of composite serial in-parallel robots," *IEEE Trans. on Robotics and Automation,* vol. 17, no. 3, pp. 301-311, June 2001.

[9] D. Kim and W. Chung, "Analytic singularity equation and analysis of six-DOF parallel manipulators using local structurization method," *IEEE Trans. on Robotics and Automation,* vol. 15, no. 4, pp. 612-622, August 1999.

[10] D. Zlatanov, R.G. Fenton and B. Benhabib, "Identification and classification of the singular configurations of mechanisms," *Mech. Mach. Theory,* vol. 33, no. 6, pp. 743-760, 1998.